Supplementary Information: Charged domain walls in improper ferroelectric hexagonal manganites and gallates

Didrik R. Småbråten,[1] Quintin N. Meier,[2] Sandra H. Skjærvø,[1]
Katherine Inzani,[1] Dennis Meier,[1] and Sverre M. Selbach[1,*]

[1] *Department of Materials Science and Engineering, Faculty of Natural Sciences and Technology, NTNU Norwegian University of Science and Technology, NO-7491 Trondheim, Norway*

[2] *Materials Theory, ETH Zurich, Wolfgang-Pauli-Strasse 27, CH-8093 Zurich, Switzerland*

(Dated: October 18, 2018)

* selbach@ntnu.no

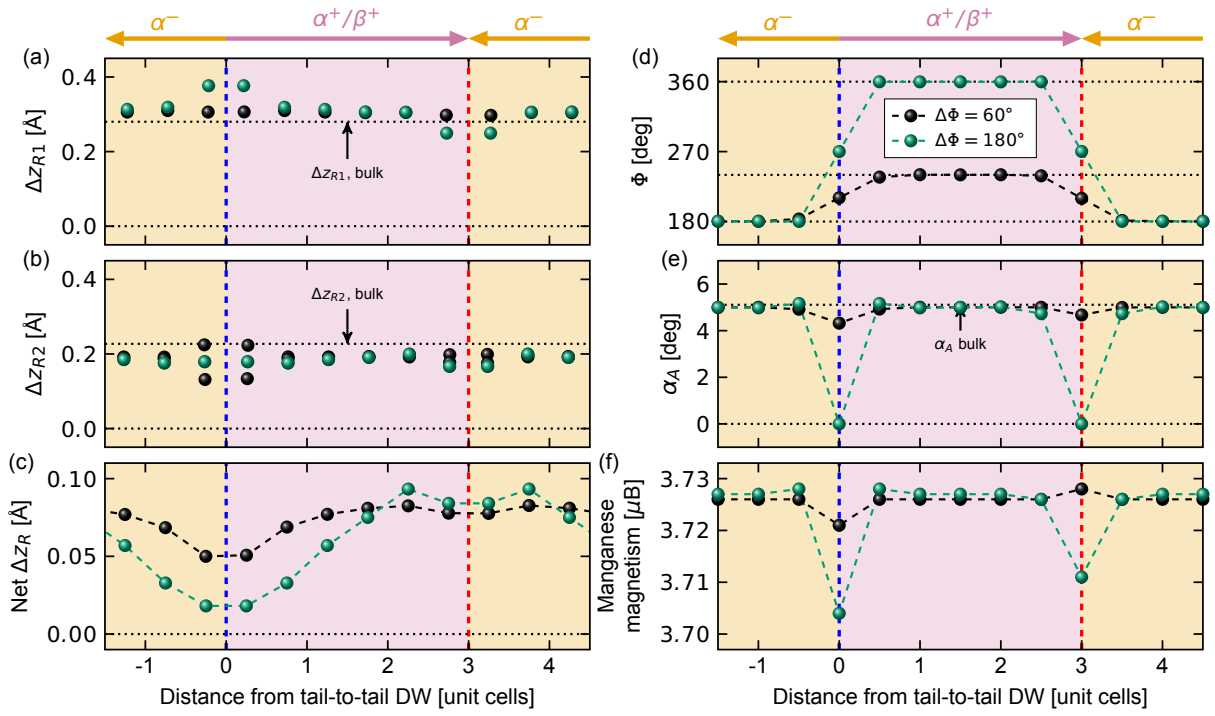

Fig. S 1. Comparison of $\Delta\Phi = 60°$ (black) and $\Delta\Phi = 180°$ (green) domain walls in $1 \times 1 \times 6$ supercells of $YMnO_3$. Evolution of R cation corrugations a) Δz_{R1}, b) Δz_{R2} and net $\Delta z_R = \sum_i \Delta z_{Ri}$, d) Φ, and e) α_A, and f) manganese magnetization.

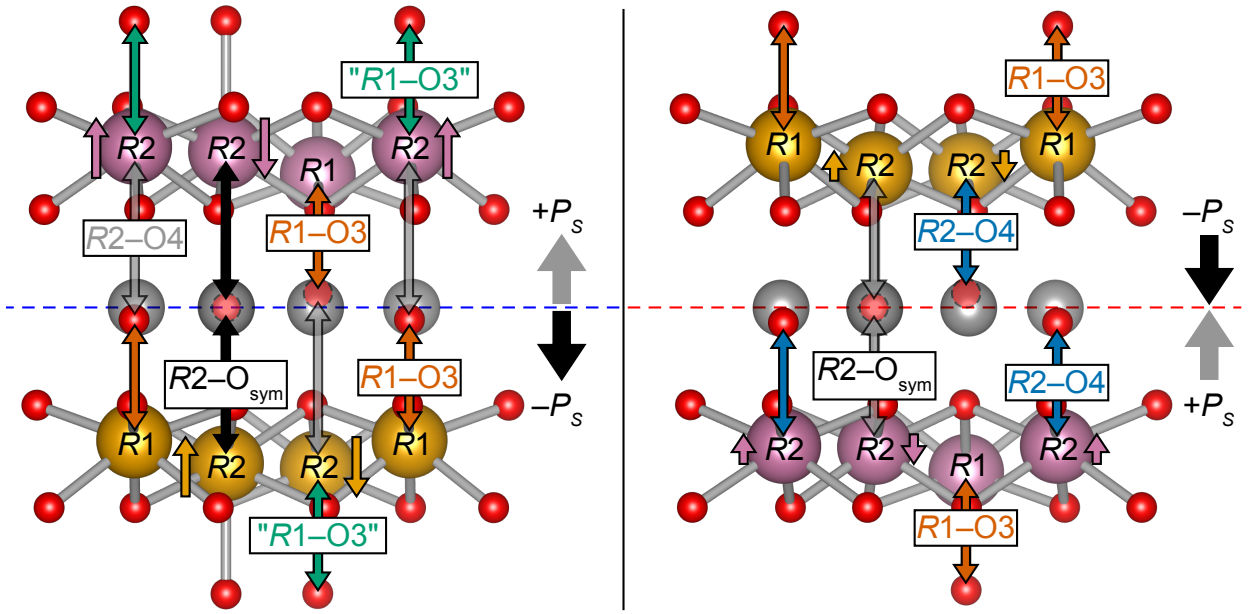

Fig. S 2. Local Y-O_7 chemical environment at tail-to-tail (left) and head-to-head (right) domain wall. $R1$-O3 (red) represents the bond between $R1$ and the closest planar O3 oxygen. "$R1$-O3" (green) represents the induced shift in $R2$ position, and resulting $R1$-O3 like behavior, in the $R1|R2$ column. $R2$-O_{symm} represents the shift in $R2$ and planar O4 oxygen positions closer to $P6_3/mmc$ in the $R2|R2$ column.

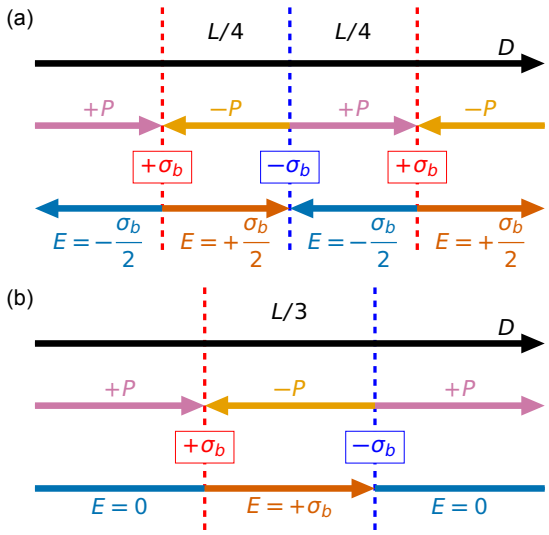

Fig. S 3. Arrays of domain walls, illustrating the difference in depolarization field assuming a) odd (or infinite) and b) even number of domain walls.

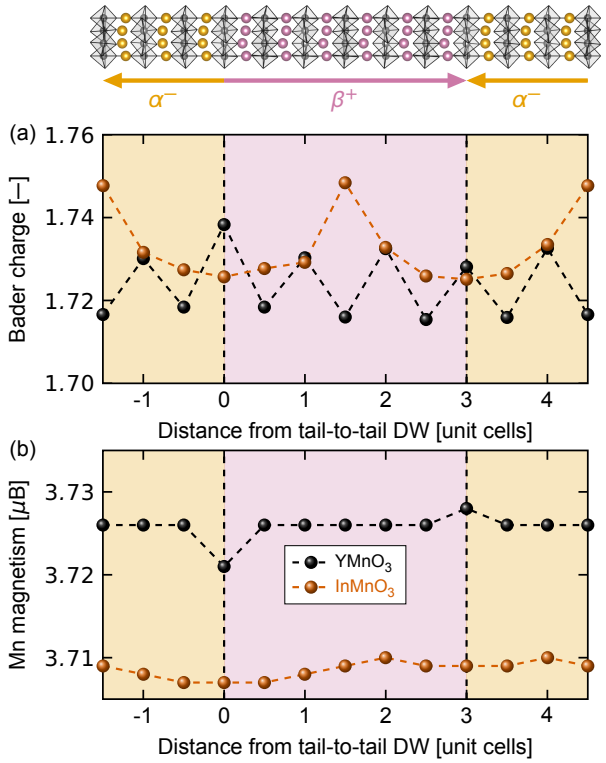

Fig. S 4. a) Bader charge analysis and b) manganese magnetism across $1\times1\times6$ $\Delta\Phi = 60°$ ($\alpha^-|\beta^+$) supercells of $YMnO_3$ (black) and $InMnO_3$ (red).

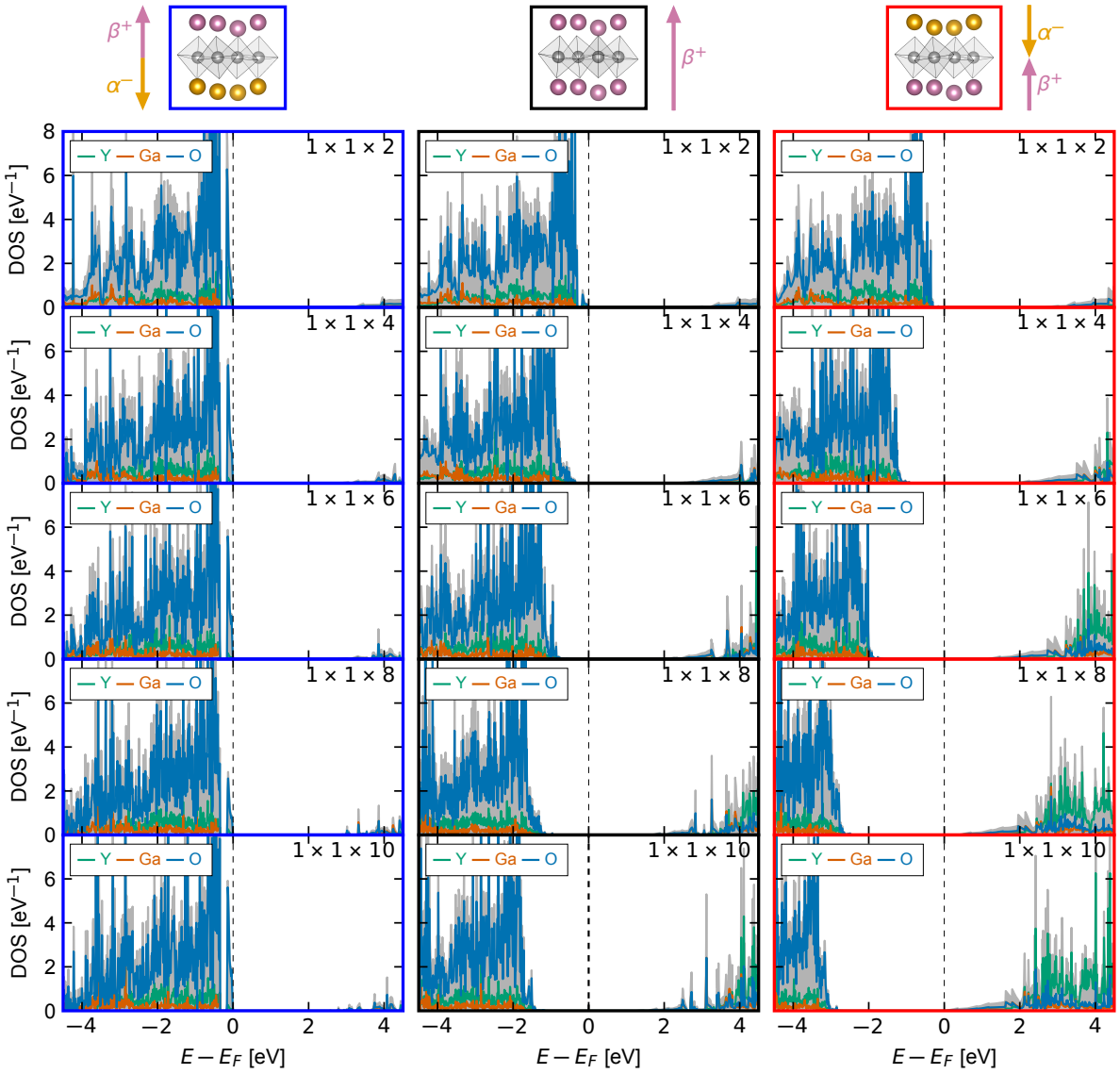

Fig. S 5. Local density of states for increasing domain wall distance in $YGaO_3$, illustrating the changes in Fermi level at tail-to-tail domain wall (blue, left), bulk (black, center) and head-to-head domain wall (red, right) for $1 \times 1 \times 2$ to $1 \times 1 \times 10$ supercell size.

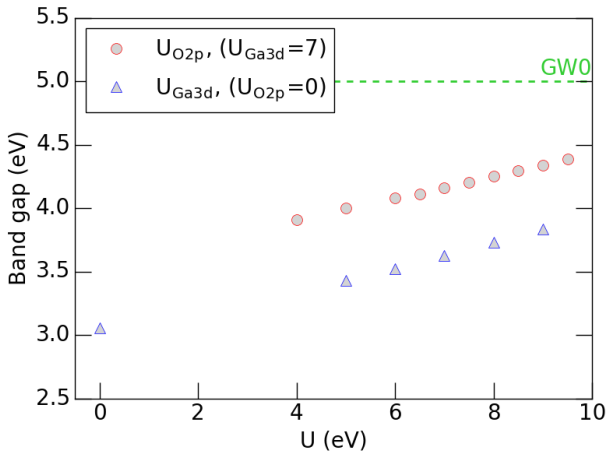

Fig. S 6. Electronic band gap of $YGaO_3$, as a function of applied U. The green dashed horizontal line represents the band gap predicted from GW_0 calculations, converging at 5.0 eV. Blue triangles represents the band gap with increasing U applied to Ga 3*d*. Red circles represents the band gap with increasing U applied to O 2*p*, with an applied U of 7 eV to Ga 3*d*.

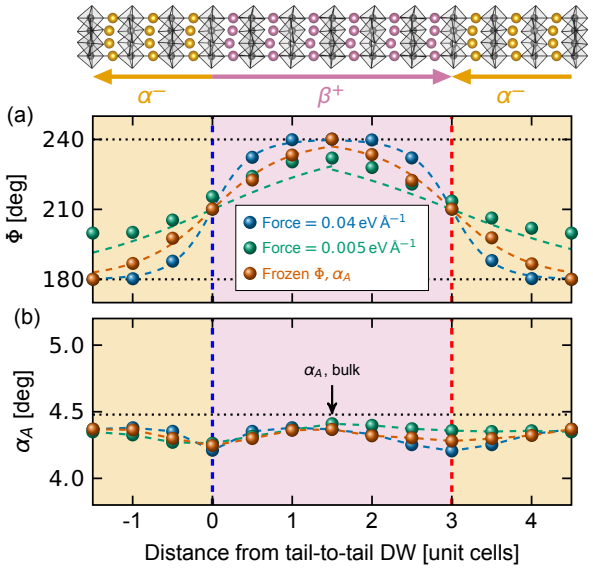

Fig. S 7. Effect of force criterion in $InMnO_3$ on the change in K_3 mode determined by changes is a) phase Φ and b) amplitude Q, for crude force criterion of 0.04 eVÅ^{-1} (blue), 0.005 eVÅ^{-1} (green) and by subsequent relaxing to 0.005 eVÅ^{-1} with the phase Φ frozen in in center of bulk after 0.04 eVÅ^{-1} relaxation.

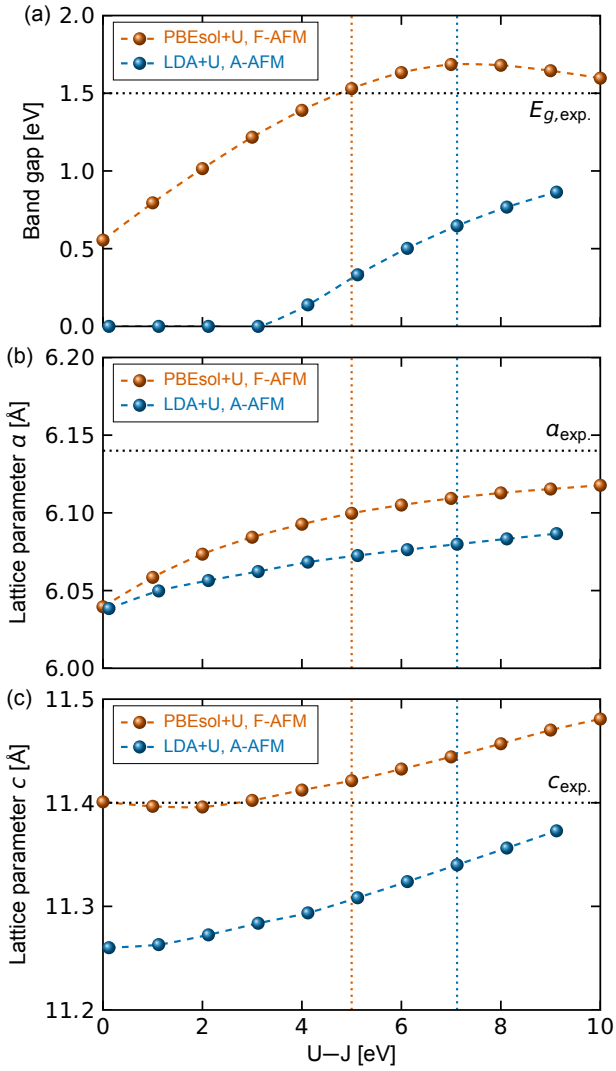

Fig. S 8. Calculated a) electronic band gap and lattice parameters b,c) a and c with respect to applied U−J, using PBEsol+U with F-AFM order (red) or LDA+U with A-AFM order (blue).

Hubbard U (and J) and magnetic order

In order to reproduce the experimental band gap and lattice parameters for $YMnO_3$ and $InMnO_3$, the choice of Hubbard U (and J) must be adjusted according to the magnetic order. For the low symmetry phase ($P6_3cm$) we use the frustrated antiferromagnetic (F-AFM) order, since this reproduces both the experimental band gap and lattice parameters (Fig. 8). A-type antiferromagnetic (A-AFM) order, on the other hand, underestimates the electronic band gap. For the high-symmetry ($P6_3/mmc$) phase, A-type antiferromagnetic (A-AFM) order is used since the unit cell of the $P6_3/mmc$ phase contains only 2 Manganese, and hence cannot capture the F-AFM order without breaking the space group symmetry.

For the DFT supercell model, reproducing *both* the lattice parameters and the experimental band gap for the low-symmetry phase is important, Hence, we used the combination of F-AFM order and an effective U−J=5 eV, resulting in an electronic band gap of $E_g = 1.53$ eV. For the *ab initio* phenomenological model, on the other hand, A-AFM order *must* be used in order to retain the space group symmetry of the high-symmetry phase. Here, LDA+U with U=8 eV and J=0.88 eV was used, which results in a band gap of the low-symmetry phase of $E_g = 0.67$ eV. These combinations of magnetic orders and self-interaction corrections are well established in the literature, see e.g. refs. [1–3].

A comparison of the calculated lattice parameters, the electronic band gap, and the energy difference between the high-symmetry and the low symmetry phase $\Delta E = E_{P6_3/mmc} - E_{P6_3cm}$ for $YMnO_3$ for the two different approaches using PBEsol+U with F-AFM order and LDA+U with A-AFM order is given in Table I. As becomes apparent, the resulting lattice parameters and energetic landscapes are similar for the two methods of choice. The only significant difference is the calculated electronic band gap. In addition, the differences in calculated phonon frequencies (in THz) in the $P6_3cm$ phase are relatively small for the two different approaches (Table II), supporting the similar crystal structure properties using either of the two methods. Here, only the low-frequency modes are shown.

TABLE I. Comparison between the calculated lattice parameters a and c, electronic band gap E_g, and energy difference between the high-symmetry and the low symmetry phase $\Delta E = E_{P6_3/mmc} - E_{P6_3cm}$ for $YMnO_3$ for the two different DFT approaches using PBEsol+U with frustrated antiferromagnetic order (F-AFM) and LDA+U with A-type antiferromagnetic order (A-AFM). Lattice parameters [4] and electronic band gap [5] from the literature are also given, for comparison.

Parameter	PBEsol+U and F-AFM	LDA+U and A-AFM	Exp.
a [Å]	6.10	6.07	6.14
c [Å]	11.42	11.34	11.40
E_g [eV]	1.53	0.67	1.5
ΔE [eV]	0.64	0.70	–

TABLE II. Comparison between the calculated low frequency phonon modes (< 10 THz) for the $P6_3cm$ phase of $YMnO_3$ for the two different DFT approaches using PBEsol+U with frustrated antiferromagnetic order (F-AFM) and LDA+U with A-type antiferromagnetic order (A-AFM).

Phonon frequencies [THz]		Phonon label
LDA+U and A-AFM	PBEsol+U and F-AFM	
-0.0278605162	-0.1379385694	Acoustic
-0.0274088225	-0.0392107078	Acoustic
3.0156891634	3.0003278	E2
3.1579077683	3.0270480681	A2
3.8451162326	3.828790988	B2
4.0704222037	3.9191548686	B1
4.3760267063	4.2682527641	E2
5.0975502188	4.9808621564	A1
5.1436213387	4.8310378826	E1
5.4590615474	5.0764043978	E1
5.484254535	4.8809716136	E2
6.173024096	6.1208904978	B2
6.3131681506	6.263927761	E1
6.319631703	6.216364405	E2
6.7279133496	6.6054643978	B2
7.1460202891	7.0827640929	E2
7.3744042491	7.1667619175	E1
7.5846980083	7.4370071442	A1
7.6391099295	7.5636673325	E2
7.7421973781	7.641040828	B1
7.9248097582	7.1678542432	E1
8.0318331208	7.7301498306	A2
8.1782788172	8.0911745537	A1
8.1804251458	7.8200581341	B1
8.239062647	8.1342585294	B2
8.898782586	7.911021652	E1
9.0175278172	8.8695409407	A2
9.2566770208	9.1549199878	E2
9.3522191363	9.2727303173	A1

Local structure and energetics of $\Delta\Phi = 180°$ domain walls

Comparison of the changes in crystal structure properties of the $\Delta\Phi = 180°$ domain wall to that of the $\Delta\Phi = 60°$ domain wall is given in Fig. 1. Here, we see an opposite trend for Δz_R, where Δz_{R2} is fairly constant across the supercell (Supp. Fig. 1b), while Δz_{R1} shows an increase at the tail-to-tail wall and a decrease at the head-to-head wall, with a corresponding reduction and increase in net Δz_R displacement, respectively (Supp. Fig. 1a). Across both domain walls, we will have one column of $R1$ meeting $R1$ and two columns of $R2$ meeting $R2$. The planar oxygen at domain wall centers will be in the high symmetry position, caused by the equal chemical environment across the interface.

The resulting $R1$-O3 bond length is expected to increase. This $R1$-O3 coupling, however, is strong, and the increased bond length is mediated by shifting $R1$ closer to the domain wall center, hence the observed increased Δz_{R1}. Similarly, at the head-to-head wall, $R1$ is again attracted towards the domain wall center to mediate the decreased $R1$-O3 bond length, with now a corresponding reduced Δz_{R1}. The amplitude α_A also drops towards zero at the center of each domain wall, corresponding to high symmetry $P6_3/mmc$-like behavior. This behavior is in accordance with reported vortex cores with emergent $U(1)$ symmetry [6, 7], where $\Delta\Phi = 180°$ across the domain wall is allowed. These large structural changes should lead to high domain wall formation energy, in agreement with our reported values. It should be noted that the $\Delta\Phi = 180°$ domain walls are modeled as flat interfaces, as for $\Delta\Phi = 60°$, however in a real material $\Delta\Phi = 180°$ are not flat interfaces, but rather points interconnecting all six domains.

Extracted parameters for the Landau model

We extracted the following parameters for the following landau free energy (For computational details see the Methods section in the paper).

$$\begin{aligned} F[Q,\Phi,\xi] = & \frac{a}{2}Q^2 + \frac{b}{4}Q^4 + \frac{Q^6}{6}(c + c'\cos 6\Phi) \\ & - gQ^3\xi\cos 3\Phi + \frac{g'}{2}\xi^2Q^2 + \frac{a_\xi}{2}\xi^2 \\ & + \sum_{i\in x,y,z} \frac{s_Q^i}{2}\left[(\partial_i Q)^2 + Q^2(\partial_i\Phi)^2\right] + \frac{s_\xi^i}{2}(\partial_i\xi)^2 \quad . \end{aligned} \tag{1}$$

TABLE III. Extracted parameters for Landau model

Material	Ω	Z	a	b	c	c'	g	g'	a_p	s_Q^z	s_ξ^z
$YGaO_3$	358.9	9.5	-3.03	5.25	0.03	0.008	2.6	12.12	1.37	19	65
$YMnO_3$	364.5	8.6	-3.21	5.65	0.70	0.03	3.2	14.6	0.93	17	53
$InMnO_3$	342.3	7.3	-0.82	1.128	0.806	0.041	1.02	4.85	3.48	12	29

Units:

V: [Å^3]

a, a_p: [$\text{eV}/\text{Å}^2$]

b, g, g': [$\text{eV}/\text{Å}^4$]

c, c': [$\text{eV}/\text{Å}^6$]

s_Q^z, s_ξ^z: [eV]

We emphasize that what we use as ξ is the displacement amplitude of the polar mode. It is directly related to the polarization by

$$P = \frac{Z\xi}{\Omega} \quad , \tag{2}$$

where Z is the mode effective charge and Ω is the unit cell volume. This lets us reformulate equation (1) in terms of P.

Derivation of equation (5)

To derive equation (5) we start from a homogeneous order parameter distribution with an applied field

$$F[Q,\Phi,P] = \frac{a}{2}Q^2 + \frac{b}{4}Q^4 + \frac{Q^6}{6}(c + c'\cos 6\Phi) \\ - g'Q^3P\cos 3\Phi + \frac{g}{2}P^2Q^2 + \frac{a_p}{2}P^2 - P\mathcal{E} \quad .$$

We minimize the free energy in respect to P, $\frac{\partial F}{\partial P} = 0$, and we find:

$$\mathcal{E} = gQ^2P - g'Q^3 + a_pP \quad . \tag{3}$$

Solving for P we retrieve the expression:

$$P = \frac{\mathcal{E} + g'Q^3}{gQ^2 + a_p} \quad . \tag{4}$$

Asymmetric chemical environment at head-to-head and tail-to-tail domain walls

Because of the change in R corrugation, there will be two $R1|R2$ columns and one $R2|R2$ column across the wall, Fig. 2. At the $R2|R2$ column, both $R2$ will will bond equally to the planar oxygen, and displace closer to high-symmetry $P6_3/mmc$ position ($\Delta z_{R2} \downarrow$). At the tail-to-tail wall, an increased $R2$-O4 bond length in the $R1|R2$ column is observed, since the planar oxygen is more strongly coupled to the adjacent $R1$ cation. This results in an increased $R2$ displacement ($\Delta z_{R2} \uparrow$) away from the wall, with more $R1$ character. This displacement propagates *away* from the wall, thus facilitating domain wall growth. Oppositely, at the head-to-head wall, $R1$ is bonded strongly to the next-neighboring Mn-O_5 layer. The adjacent $R2$-O4 bond length is less affected by the change in corrugation, and a smaller change in $R2$ displacement is observed. This displacement propagates *towards* the wall, thus screening domain wall growth.

Arrays of domain walls

Finite arrays. We want to discuss the addition of electric fields in arrays of domain walls from finite arrays to periodic boundary conditions, while assuming that the domain walls are infinite sheets with a charge density of $\pm\sigma$.

A single domain wall at a coordinate x_0 thus creates an electric field $\mathcal{E}$ of

$$\mathcal{E} = \frac{\sigma}{2} sign(x_0) \quad , \tag{5}$$

where *sign* is the signums function, showing the change of sign left or right from the wall. It becomes immediately clear, that adding a second charged domain wall will create a capacitor-like geometry with an effective field $\mathcal{E} = \sigma$ in between and $\mathcal{E} = 0$ outside the two walls. Adding a third wall will then immediately lead to the situation where we have alternating $\pm\sigma_b$.

Infinite arrays. The electric field in an infinite array of domain walls is non-trivial, and we will systematically build this and take the infinite limit. For the electric potential not to diverge, the only solution is the one for uneven number of arrays. We can calculate this in the following way: without loss of generality we decide to start with a mono-domain with polarization of $-P$.

The first domain wall we add on the right-hand side leads to a field of $\frac{\sigma_b}{2}$, the second one to a field of $\frac{-\sigma_b}{2}$ and so on. Thus we find that

$$\mathcal{E} = \underbrace{\frac{\sigma_b}{2}\sum_{n=0}^{\infty}(-1)^n}_{left} + \frac{\sigma_b}{2}\sum_{n=0}^{\infty}(-1)^n \quad . \tag{6}$$

While this sum is diverging, we can use dirichlet regularization to calculate its limit, thus using

$$\lim_{s\to 0}\left(\sum_{n=0}^{\infty}(-1)^n n^{-s}\right) = \frac{1}{2} \quad . \tag{7}$$

We find that

$$\mathcal{E} = \frac{\sigma_b}{2} \quad . \tag{8}$$

Thus the infinite limit is equal to the case of an odd number of domain walls.

Bulk material properties

Using GGA+U[8] with U of 5 eV applied to Mn $3d$ and PBEsol functional[9], $YMnO_3$ and $InMnO_3$ have calculated band gaps of 1.53 eV and 1.43 eV, respectively. Here, the Hubbard-U value is chosen to reproduce the experimental band gap[5, 10]. $YGaO_3$ has, to the authors knowledge, no reported experimental band gap. $YGaO_3$ calculations were performed *without* Hubbard U, resulting in a band gap of 3.1 eV. Since Ga has filled $3d$ sates it seems counter intuitive to apply U on these states. This procedure also reproduced the experimental lattice parameters (Fig 6). From GW_0 calculations, the band gap is found to converge at 5.0 eV, with five iterations converged within 0.01 eV, Fig. 6. Testing with both U applied to Ga $3d$, as well as O $2p$, did not reach the predicted GW_0 band gap within reasonable choices of U value (Fig 6). Since we emphasize the *qualitative trend* with increasing band gap, a band gap of 3.1 eV should be sufficient.

The polarization of $YMnO_3$ and $YGaO_3$ are calculated to 7.05 μC cm^{-2} and 6.72 μC cm^{-2}, while $InMnO_3$ has a calculated polarization of 3.64 μC cm^{-2} from a simple point charge model using formal charges for 30 atom supercell. We report our DFT relaxed polarizations from this point charge model with formal charges. From Berry phase method [11], we get polarizations of 7.34 μC cm^{-2} ($YMnO_3$), 3.37 μC cm^{-2} ($InMnO_3$) and 6.67 μC cm^{-2} ($YGaO_3$), which are close to the ones from the aforementioned point charge model.

DFT relaxed $InMnO_3$ supercells

Because of the more covalent In-O_p bonding in $InMnO_3$[12] compared to the more ionic Y-O_p bond, this results in an inherently smaller amplitude of Q and weaker coupling term to P in this material. It is shown [12, 13] that in $InMnO_3$ there will be a competition between the ferroelectric $P6_3cm$ and the non-polar $P\bar{3}c1$ structure. From symmetry, the domain wall will, in principle, adopt the $P\bar{3}c1$ structure. However, from strain field in the proximity of the wall, the symmetry is lowered to $P3c1$, a subgroup of both polar and non-polar symmetries. This is apparent since none of the ions relax to the high-symmetry position close to and at the walls.

If we calculate the energy difference between the bulk $P6_3cm$ and $P\bar{3}c1$ configurations, $\Delta E = E^f_{P\bar{3}c1} - E^f_{P6_3cm}$, we find ΔE values of 23.35 meV/f.u. ($YMnO_3$) and 18.45 meV/f.u.

($YGaO_3$) for the Y compounds, while $InMnO_3$, has one order of magnitude lower ΔE value of 1.76 meV/f.u.. The stability of $P6_3cm$ and $P\bar{3}c1$ phases in $InMnO_3$ are very similar[12, 13], and because of this flat energy landscape of the hettotype phases in $InMnO_3$, there will be a competition between forming a $P\bar{3}c1$ monodomain, or two $P6_3cm$ domains separated by two domain walls. This is apparent in Fig. 7, where the supercell slowly converges towards a $P\bar{3}c1$ monodomain state, when using the same force criterion (0.005 eV/Å) as for the Y-compounds. To converge to the two-domain state, we first relaxed the supercell with a crude force criterion (0.04 eVÅ), and subsequently froze in Φ and α_A at center of the domains, and relaxed with the strict force criterion.

Local charge compensation of charged domain walls

The screening of the bound positive and negative charges at the head-to-head and tail-to-tail DWs is expected to be realized by partial reduction of Mn^{3+} to Mn^{2+} and oxidation of Mn^{3+} to Mn^{4+}, respectively. The local charge compensation in $1\times1\times6$ ($\alpha^-|\beta^+$) supercells of $YMnO_3$ and $InMnO_3$ can be indicated by changes in manganese magnetization and changes in calculated Bader charges (Fig. 4). A decrease in magnetic moment indicate more Mn^{4+} character, and increase more Mn^{2+} character, and oppositely for the Bader charges. From the magnetic moments in Fig. 4, we observe to some degree partial charge compensation of the domain walls by oxidizing or reducing manganese. For $YMnO_3$, the planar averaged Mn magnetic moments follow a stepwise increase from 3.726 μB in bulk to 3.728 μB at the head-to-head DW centre, and a stepwise reduction to 3.721 μB at the tail-to-tail DW centre. However, these changes are subtle, as is apparent from the Bader charges, Fig. 4, where no apparent trend is observed. In addition, integrated DOSes of the occupied states in the conduction band at the head-to-head wall, and the unoccupied states above the valence band edge at the tail-to-tail wall, reveal a charge transfer of $\sim 0.02\ e^-/h^+$ between the two walls. It is to be noted that these changes will also depend on the supercell size, and more quantitative clear trends are expected with increasing wall distance.

[1] J. E. Medvedeva, V. I. Anisimov, M. A. Korotin, O. N. Mryasov, and A. J. Freeman, J. Phys. Condens. Matter **12**, 4947 (2000).

[2] Y. Kumagai and N. A. Spaldin, Nat. Commun. **4**, 1540 (2013).

[3] S. H. Skjærvø, E. T. Wefring, S. K. Nesdal, N. H. Gaukås, G. H. Olsen, J. Glaum, T. Tybell, and S. M. Selbach, Nat. Commun. **7**, 13745 (2016).

[4] A. S. Gibbs, K. S. Knight, and P. Lightfoot, Phys. Rev. B **83**, 094111 (2011).

[5] C. Degenhardt, M. Fiebig, D. Fröhlich, T. Lottermoser, and R. Pisarev, Appl. Phys. B **73**, 139 (2001).

[6] Q. Zhang, G. Tan, L. Gu, Y. Yao, C. Jin, Y. Wang, X. Duan, and R. Yu, Sci. Rep. **3**, 2741 (2013).

[7] M. E. Holtz, K. Shapovalov, J. A. Mundy, C. S. Chang, Z. Yan, E. Bourret, D. A. Muller, D. Meier, and A. Cano, Nano Lett. **17**, 5883 (2017).

[8] S. L. Dudarev, G. A. Botton, S. Y. Savrasov, C. J. Humphreys, and A. P. Sutton, Phys. Rev. B **57**, 1505 (1998).

[9] J. P. Perdew, A. Ruzsinszky, G. I. Csonka, O. A. Vydrov, G. E. Scuseria, L. A. Constantin, X. Zhou, and K. Burke, Phys. Rev. Lett. **100**, 136406 (2008).

[10] A. M. Kalashnikova and R. V. Pisarev, J. Exp. Theor. Phys. **78**, 143 (2003).

[11] N. A. Spaldin, J. Solid State Chem. **195**, 2 (2012).

[12] Y. Kumagai, A. A. Belik, M. Lilienblum, N. Leo, M. Fiebig, and N. A. Spaldin, Phys. Rev. B **85**, 174422 (2012).

[13] S. M. Griffin, M. Reidulff, S. M. Selbach, and N. A. Spaldin, Chem. Mater. **29**, 2425 (2017).